Journal of Vacuum Science and Technology A

RESEARCH ARTICLE | FEBRUARY 01 2024

Impact of high-power impulse magnetron sputtering pulse width on the nucleation, crystallization, microstructure, and ferroelectric properties of hafnium oxide thin films

Samantha T. Jaszewski ; Shelby S. Fields ; Ching-Chang Chung; Jacob L. Jones ; Keithen G. Orson ; Petra Reinke ; Jon F. Ihlefeld

J. Vac. Sci. Technol. A 42, 023414 (2024)
https://doi.org/10.1116/6.0003307

27 July 2024 19:55:05

ARTICLE

pubs.aip.org/avs/jva

Impact of high-power impulse magnetron sputtering pulse width on the nucleation, crystallization, microstructure, and ferroelectric properties of hafnium oxide thin films

Cite as: J. Vac. Sci. Technol. A **42**, 023414 (2024); doi: 10.1116/6.0003307
Submitted: 16 November 2023 · Accepted: 22 December 2023 ·
Published Online: 1 February 2024

View Online

Export Citation

CrossMark

Samantha T. Jaszewski,[1,2,a)] Shelby S. Fields,[1] Ching-Chang Chung,[3] Jacob L. Jones,[3] Keithen G. Orson,[1] Petra Reinke,[1] and Jon F. Ihlefeld[1,4,b)]

AFFILIATIONS

[1] Department of Materials Science and Engineering, University of Virginia, Charlottesville, Virginia 22904
[2] Sandia National Laboratories, Albuquerque, New Mexico 87185
[3] Department of Materials Science and Engineering, North Carolina State University, Raleigh, North Carolina 27695
[4] Charles L. Brown Department of Electrical and Computer Engineering, University of Virginia, Charlottesville, Virginia 22904

[a)] **Author to whom correspondence should be addressed:** stj6ze@virginia.edu
[b)] **Electronic mail:** jihlefeld@virginia.edu

27 July 2024 19:55:05

ABSTRACT

The impact of the high-power impulse magnetron sputtering (HiPIMS) pulse width on the crystallization, microstructure, and ferroelectric properties of undoped HfO_2 films is investigated. HfO_2 films were sputtered from a hafnium metal target in an Ar/O_2 atmosphere, varying the instantaneous power density by changing the HiPIMS pulse width with fixed time-averaged power and pulse frequency. The pulse width is shown to affect the ion-to-neutral ratio in the depositing species with the shortest pulse durations leading to the highest ion fraction. *In situ* x-ray diffraction measurements during crystallization demonstrate that the HiPIMS pulse width impacts nucleation and phase formation, with an intermediate pulse width of 110 μs stabilizing the ferroelectric phase over the widest temperature range. Although the pulse width impacts the grain size with the lowest pulse width resulting in the largest grain size, the grain size does not strongly correlate with the phase content or ferroelectric behavior in these films. These results suggest that precise control over the energetics of the depositing species may be beneficial for forming the ferroelectric phase in this material.

Published under an exclusive license by the AVS. https://doi.org/10.1116/6.0003307

I. INTRODUCTION

Since the first report of ferroelectricity in SiO_2-doped hafnium oxide (HfO_2) thin films in 2011,[1] interest in this material has grown for several microelectronic applications. In particular, ferroelectric HfO_2 is a promising candidate for nonvolatile memory devices like ferroelectric random-access memory because it is thermodynamically compatible with silicon[2] and has the potential to overcome some of the limitations of existing nonvolatile memory, such as limited scaling and high-power consumption. Atomic layer deposition (ALD) is the most widely used technique for the fabrication of HfO_2-based thin films, although chemical solution deposition, pulsed laser deposition (PLD), and sputtering have also been explored.[3] In comparison with ALD, sputter deposition offers a wider range of processing parameters that can be used to tailor film properties. Still, conventional sputter techniques have limited means to control the energy of the depositing species, so techniques like high-power impulse magnetron sputtering (HiPIMS) that have a wider processing space merit exploration for the deposition of ferroelectric HfO_2-based thin films.

HiPIMS is a physical vapor deposition (PVD) technique in which low duty cycle pulses (<5% duty cycle) are applied to a sputter target to produce dense plasmas with a high degree of sputtered atom ionization.[4,5] This ionization can be controlled by varying pulse parameters such as pulse width, frequency, and

Published under an exclusive license by the AVS

voltage. The high degree of sputtered atom ionization and the resulting ion bombardment during deposition enables access to regions of the structure zone diagram where equiaxed nanocrystalline microstructures result, whereas traditional sputtering techniques are restricted to lower energy regions of the structure zone model and, thus, are limited in their ability to control microstructural features, such as the grain size.[6] As an example, CrN films prepared by DC sputtering have a porous columnar morphology, while HiPIMS results in a uniform, dense, equiaxed nanocrystalline structure.[7] Control over the microstructure may be beneficial for HfO_2 thin films where the grain size has been linked to the stability of the ferroelectric phase, with the ferroelectric orthorhombic phase (space group $Pca2_1$) stabilized by intermediate grain size in comparison with the tetragonal (space group $P4_2/nmc$) and monoclinic (space group $P2_1/c$) phases.[8,9] In addition to the pulse parameters, background pressure and gas atmosphere can be controlled during HiPIMS; these parameters can be utilized to tailor the ion energy and flux of the depositing species, thus providing additional control over the film's microstructure and properties in comparison with conventional ALD and PVD processes.

In this work, the effect of the HiPIMS pulse width on the phase nucleation, crystallization, microstructure, and ferroelectric properties will be explored. By varying the HiPIMS pulse width, different instantaneous power densities and positive ion-to-neutral ratios are obtained. To assess the effects of this parameter on crystallization behavior and phase stability, *in situ* x-ray diffraction (XRD) patterns are measured and compared to grazing-incidence XRD measurements of films that underwent a rapid thermal anneal (RTA). In order to maximize the signal for the *in situ* XRD measurements, a film thickness of 20 nm is chosen for HfO_2. The microstructure is examined by taking plan-view scanning electron microscopy (SEM) images and atomic force microscopy (AFM) images. While differences in the grain size between films are observed, these differences cannot account for the changes in phase formation and ferroelectric properties that are measured for the different pulse widths.

II. EXPERIMENT

A. Deposition parameters

20 nm thick HfO_2 films were deposited on 100 nm thick TaN films on (001)-oriented *p*-type silicon substrates. The TaN was deposited via pulsed DC-magnetron sputtering in a Denton Discovery 550 system (30 kHz, 4 μs reverse time) from a TaN target. HfO_2 films were sputtered from a 50 mm diameter hafnium metal target of 99.9% purity (excluding zirconium impurities) as described in previous work.[10] A Starfire Impulse HiPIMS power module and DC power supply were used for HiPIMS depositions. HiPIMS pulses ranged from 50 to 140 μs in width, at a frequency of 200 Hz. After each negative high-power pulse, a +100 V, 200 μs pulse was applied to the target. The HfO_2 films were sputtered in a reactive environment with argon and O_2 gases. A gas flow of 15.00 SCCM of argon and varying O_2 flow rates were used with a constant background pressure of 5 mTorr. The substrate platen was grounded, not intentionally heated, and rotated during the depositions.

Following deposition, one set of films was left as-deposited for *in situ* high-temperature XRD measurements, while another set of films was annealed at 800 °C for 30 s in an argon atmosphere (99.999% purity) using an Allwin 21, Heatwave AW 610 rapid thermal processor. The ramp rate was 66.7 °C/s. Last, circular electrodes consisting of 20 nm of titanium nitride and 50 nm of palladium were DC-magnetron sputtered through a shadow mask to create a capacitor structure for electrical measurements. Further details are provided in previous work.[10]

B. Characterization

The HiPIMS waveforms were extracted from an oscilloscope connected to the voltage and current monitor outputs of the Starfire Impulse module in order to measure the instantaneous voltage and currents during the deposition. Positive ion-to-neutral ratios were measured using the quartz crystal microbalance on an Impedans Quantum Retarding Field Ion Energy Analyzer with grid potentials varied to first block electrons and negative ions from reaching the sensor and then all ions by increasing the positive grid bias to 150 V. By taking the ratio of the deposition rates with and without ions, the positive ion-to-neutral ratio was calculated.

X-ray photoelectron spectroscopy (XPS) spectra were measured with a Scienta Omicron Multiprobe MXPS system with an XM1200 monochromator. Monochromatic Al K_α ($h\nu = 1486.6$ eV) radiation was used to acquire the spectra. Survey spectra were measured with a pass energy of 100 eV, while core level spectra were measured with a pass energy of 25 eV and energy steps of 0.05 eV. KolXPD software was used to analyze the data.[11] A Shirley background was chosen, and Voigt functions were used to fit core levels.[12] The peak areas for each core level were corrected using cross sections provided by Scofield.[13] Then, the stoichiometries of the films were calculated by taking the ratio of the corrected area of the O 1*s* peak attributed to lattice Hf–O bonding to the corrected areas of the Hf $4f_{5/2}$ and Hf $4f_{7/2}$ peaks.

27 July 2024 19:55:05

A Rigaku Smartlab x-ray diffractometer with Cu K_α radiation in a parallel beam configuration was used for in-plane XRD measurements and out-of-plane grazing-incidence x-ray diffraction (GIXRD) measurements with a fixed incident angle of 0.7°. The 2θ range of 26°–33° used for these measurements includes 100% intensity reflections of the monoclinic $P2_1/c$ phase, tetragonal $P4_2/nmc$ phase, antipolar orthorhombic *Pbca* phase, and orthorhombic $Pca2_1$ phase. Scherrer's equation[14] was used to calculate the crystallite size following correction for instrumental broadening effects using Standard Reference Material® 660c lanthanum hexaboride powder from the National Institute of Standards and Technology.[15] *In situ* high-temperature XRD measurements were used to assess phase evolution during crystallization. These measurements were made on a PANalytical Empyrean x-ray diffractometer with Cu K_α radiation in a Bragg–Brentano geometry with a linear detector and an Anton Paar HTK1200 high-temperature stage. Similar to prior studies of the crystallization of HfO_2-based thin films,[16,17] the samples were heated at a rate of 2 °C/min from 25 to 1000 °C in a nitrogen environment, and diffraction patterns were collected every 6 °C.

Electrical characterization was performed after field cycling at 1 kHz with 5000 3 MV/cm square waves. $P(E)$ measurements with a period of 10 ms (100 Hz equivalent frequency) were made on a Radiant Technologies Precision LC II Ferroelectric Property Analyzer.

Published under an exclusive license by the AVS

To analyze the microstructure of the films, SEM and AFM were used. Plan-view SEM images were acquired in an FEI Helios UC G4 microscope in the secondary electron mode with a through-the-lens detector. The accelerating voltage was 2.00 kV, the beam current was 0.1 nA, the dwell time was 15 μs, and the working distance was 2.3 mm. Topographic AFM images were obtained in an Oxford Instruments Asylum Research Cypher-S instrument in the AC tapping mode equipped with NanoSensor PPP-NCHR-10 probes with a resonance frequency of 190 kHz.

III. RESULTS AND DISCUSSION

A. HiPIMS conditions

Four 20 nm thick HfO_2 films were deposited via HiPIMS with pulse widths of 50, 80, 110, and 140 μs with corresponding instantaneous power densities of 1023–568 W/cm^2, as shown in Table I. The instantaneous powers were calculated using HiPIMS voltage and current waveforms. For all pulse width conditions, these waveforms were monitored to avoid the target poisoning regime in which the current sharply increases without saturating. Target poisoning should be avoided as it affects the sputter yield and secondary electron emission yield.[18,19] As the pulse width was decreased, the pulse voltage and current increased since the time-averaged power was kept constant at 200 W. Thus, the 50 μs pulse width had the highest instantaneous power of 1023 W/cm^2. Previous work has shown that the properties of HfO_2 thin films are highly sensitive to the oxygen content, and small changes in the plasma oxygen content during HiPIMS deposition can produce large differences in the film oxygen content.[10] Thus, it was important to ensure that the oxygen content in the films was controlled so that the effects of the HiPIMS pulse width could be evaluated in isolation. For each pulse width, a different oxygen flow rate was chosen so that the films would have a similar oxygen content. A lower plasma oxygen content was chosen for lower pulse widths to avoid target poisoning since target poisoning occurs during the “off state” of the plasma, and shorter pulses have longer off times.[20,21] XPS measurements were performed to assess the oxygen content in the films after crystallization, and the stoichiometries are shown in Table I. The Hf 4*f* and O 1*s* core levels that were fit to obtain these compositions are shown in Fig. 1. The O 1*s* spectra consist of two peaks: one at approximately 531 eV resulting from lattice oxygen, and the other at approximately 533 eV resulting from adventitious hydroxyls and

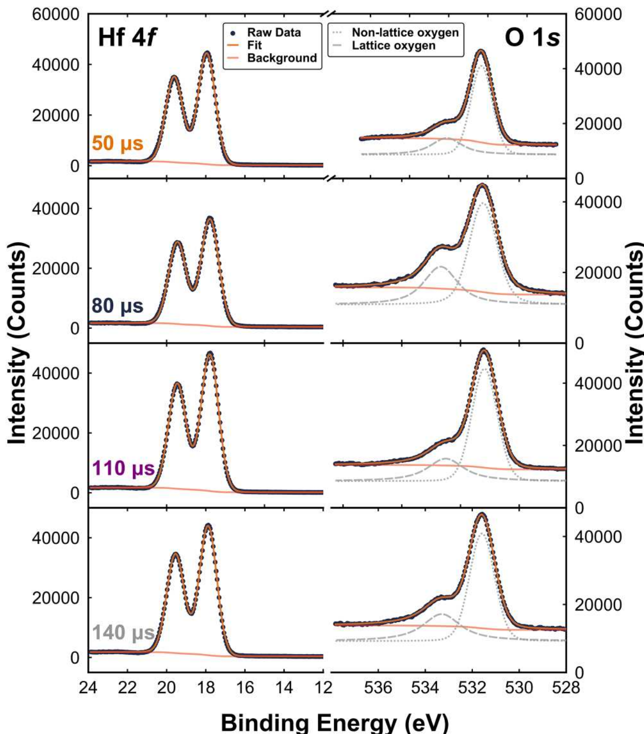

FIG. 1. Hf 4*f* and O 1*s* XPS spectra for the HfO_2 films deposited with 50, 80, 110, and 140 μs pulse widths. The spectra were fit using KolXPD software.

water adsorbed on the surface of the film under ambient conditions. Only the O 1*s* signal resulting from lattice oxygen was used in the composition calculations. No Hf^{3+} signature that would be present on the low binding energy side of the Hf $4f_{7/2}$ peak is evident in these spectra.[22] The absence of an Hf^{3+} signal indicates that there is not a significant fraction of charged vacancies in these films, although the films are oxygen deficient according to the calculations of the film oxygen content. This result is consistent with prior measurements on HiPIMS-prepared hafnia films.[10]

The positive ion-to-neutral ratio measured during the deposition for each HiPIMS pulse width is shown in Fig. 2. Previous studies have shown that shorter HiPIMS pulse widths result in higher ionization fractions.[23,24] Similarly, here, it is demonstrated that the shortest pulse width of 50 μs results in the highest positive ion-to-neutral ratio of 0.73. A nearly linear decrease leading to a reduction in the ion-to-neutral ratio by nearly a factor of two is observed as the pulse width increases, and the 140 μs sample has the lowest ratio of 0.39. The measurements confirm that a shorter pulse width, which corresponds to a higher instantaneous power, results in a larger fraction of positive ions in the plasma. Since each negative pulse is followed by a 100 V positive pulse, a lower pulse width with a larger fraction of positive ions would result in an increase in the number of ions bombarding the growing film as the 100 V pulse provides a stimulus to drive positive ions toward the substrate.

TABLE I. Pulse width, pulse frequency, and plasma oxygen content used for the deposition of the HfO_2 films, and the resulting instantaneous power and film oxygen content measured by XPS.

Pulse width (μs)	Pulse frequency (Hz)	Instantaneous power density (W/cm^2)	Plasma oxygen content (%)	Film oxygen content (x in HfO_x)
50	200	1023	7.1	1.48
80	200	696	7.6	1.61
110	200	602	7.6	1.52
140	200	568	8.8	1.44

27 July 2024 19:55:05

Published under an exclusive license by the AVS

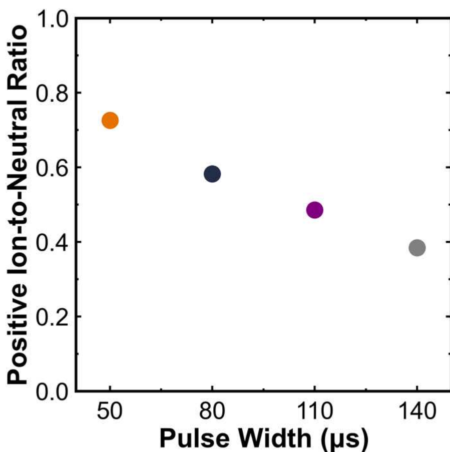

FIG. 2. Positive ion-to-neutral ratio calculated from the deposition rates of positive ions + neutrals to neutrals alone.

B. X-ray diffraction characterization

To assess the impact of the HiPIMS pulse width on the structural evolution of HfO_2 thin films, *in situ* high-temperature XRD measurements were performed. Figure 3 shows the *in situ* high-temperature x-ray diffraction patterns for the films that are amorphous as deposited. All of the films begin to crystallize at around 500 °C. For the 50 and 80 μs samples, the formation of the polar orthorhombic (111), antipolar orthorhombic (211), and/or tetragonal (101) peaks occurs at approximately 500 °C along with the formation of the monoclinic $(\bar{1}11)$ peak. The crystallization temperature of the monoclinic phase in these samples differs from that of the 110 μs sample in which the monoclinic phase does not begin to crystallize until much higher temperatures. Once again, for the 140 μs sample, the crystallization of the monoclinic phase occurs at a similar temperature to that of the orthorhombic and/or tetragonal phase. In addition, the orthorhombic and/or tetragonal phases are stable from 500 to 900 °C for the films deposited with 110 and 140 μs pulse widths, while these phases are only stable from 500 to 800 °C for films deposited with 50 and 80 μs pulse widths. Although the film oxygen content does not vary within experimental error between the films, the presence of oxygen impurities in the nitrogen gas, desorption from the furnace insulation, and desorption from the alumina sample stage and sample holder during these measurements likely eliminated any differences in the original oxygen content within the films and made them less oxygen deficient. Therefore, the differences in crystallization between samples cannot be attributed to variations in the oxygen content. These results demonstrate that phase formation is being impacted by the HiPIMS pulse width. However, it should be noted that the rate of heating used for these experiments (2 °C/min) is significantly slower than a typical rapid thermal anneal process to account for the XRD acquisition time.

The crystallization behavior observed in the *in situ* XRD experiment was compared to films that underwent RTA that is more typically used to crystallize ferroelectric HfO_2 thin films. Figure 4 shows the GIXRD patterns for identical films that have undergone rapid thermal annealing at 800 °C with a heating rate of 67 °C/s. The relative orthorhombic + tetragonal (o + t) phase fractions are approximated by fitting the GIXRD patterns using LIPRAS fitting software[25] and taking the ratio of the integrated peak intensity of the orthorhombic + tetragonal peak to the integrated intensity sum of all three peaks. The peak intensity ratio is used to approximate the phase fraction because the structure factors and multiplicities of these families of reflections for these phases are comparable. This approximation also assumes that there are no significant preferred orientation effects. The 50 μs film has the smallest fraction of the orthorhombic + tetragonal phase (0.33 ± 0.07) and predominantly consists of the monoclinic phase. The 80 μs film contains more orthorhombic/tetragonal phase (0.51 ± 0.04) but still has a significant fraction of the monoclinic phase. The 110 μs

27 July 2024 19:55:05

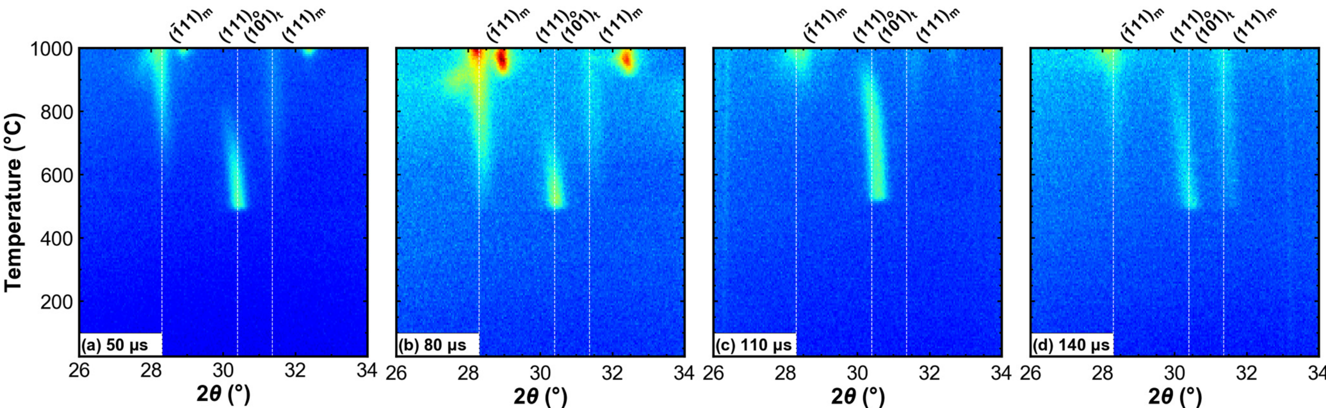

FIG. 3. *In situ* high-temperature XRD measurements of films deposited with (a) 50, (b) 80, (c) 110, and (d) 140 μs pulse widths. Similar crystallization behavior is observed for the 50, 80, and 140 μs samples, while a significantly higher crystallization temperature of the monoclinic phase (~850 °C) is noted for the 110 μs sample.

Published under an exclusive license by the AVS

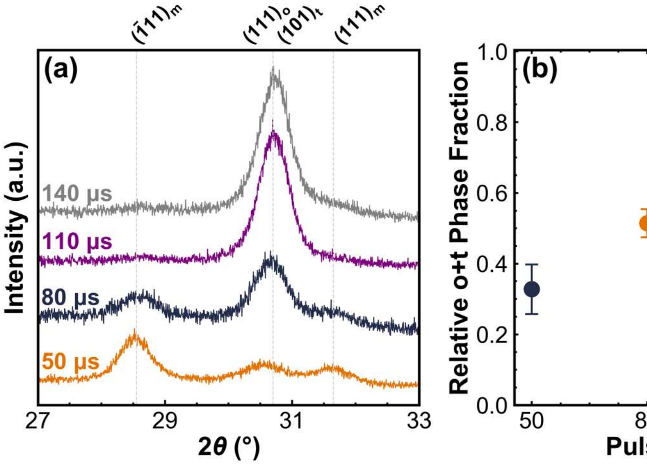

FIG. 4. (a) GIXRD patterns for films deposited with 50, 80, 110, and 140 μs pulse widths, rapid thermal annealed at 800 °C, and the (b) relative o + t phase fractions calculated from the GIXRD measurements.

sample has the highest fraction of the orthorhombic + tetragonal phase (0.94 ± 0.03), and together with the 140 μs sample, these films primarily consist of the orthorhombic and/or tetragonal phases.

It has been reported that the heating rate used during annealing can significantly affect the phases that form in HfO_2 thin films, with greater fractions of the monoclinic phase forming at 10 °C/s than at 66 °C/s;[26] however, in this case, these results are consistent with the *in situ* diffraction measurements shown above. The lower pulse widths result in large fractions of the monoclinic phase, while the 110 μs pulse width has the highest fraction of metastable phases. Similarly, in the *in situ* diffraction measurements, the monoclinic phase dominates at the temperature used for the rapid thermal anneal (800 °C) for the lower pulse width, whereas the o + t phase dominates for the 110 μs sample. The similar results obtained through drastically different heating rates provide additional evidence that the HiPIMS pulse width is impacting nucleation and is an important variable to consider when tailoring deposition conditions to obtain phase-pure films.

C. Electrical characterization

In order to assess how the pulse width and phase content affect ferroelectric properties, the polarization-electric field responses of the films after field cycling with 5000 3.0 MV/cm 1 kHz square waves were measured and are shown in Fig. 5. At the lower pulse widths of 50 and 80 μs, the hysteresis loops open very little and have remanent polarization (P_r) values of 1.9 and 3.6 μC/cm^2, respectively. The low P_r values can be explained by the dominating linear dielectric response of the significant fraction of the monoclinic phase in these films. At the higher pulse widths, however, the hysteresis loops are more open and exhibit a polarization response typical of the ferroelectric orthorhombic phase. The 110 μs film has the largest hysteretic response, with a P_r of 9.4 μC/cm^2, which correlates with the large fraction of the orthorhombic phase observed in the GIXRD measurements. The 140 μs film has the second largest P_r of 4.4 μC/cm^2. Combined with the XRD results, these measurements suggest that the 110 μs pulse width condition results in the highest fraction of the ferroelectric phase in these films.

27 July 2024 19:55:05

D. Crystallite size and microstructure

To determine whether the difference in polarization hysteresis behavior is linked to microstructure, the crystallite size and grain sizes of the films were evaluated through analysis of XRD data, SEM images, and AFM images. In-plane XRD measurements were performed so that the crystallite sizes could be further assessed, and the patterns are shown in Fig. 6. The crystallite sizes calculated using Scherrer's equation from out-of-plane and in-plane XRD measurements are shown in Fig. 7. Both out-of-plane and in-plane measurements show that the pulse width has an effect on the crystallite size. The 50 μs sample had the lowest in-plane and out-of-plane crystallite sizes. It should be noted that the

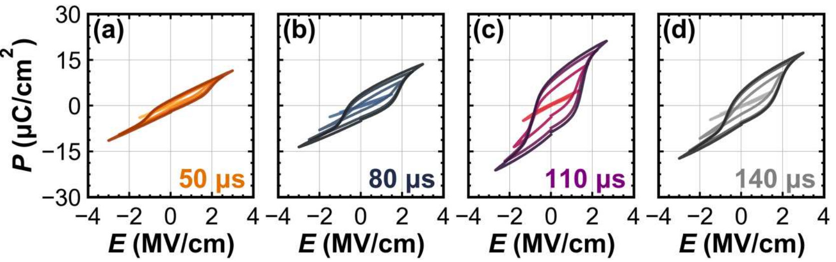

FIG. 5. Nested polarization hysteresis measurements after field cycling for the samples deposited with (a) 50, (b) 80, (c) 110, and (d) 140 μs pulse widths.

Published under an exclusive license by the AVS

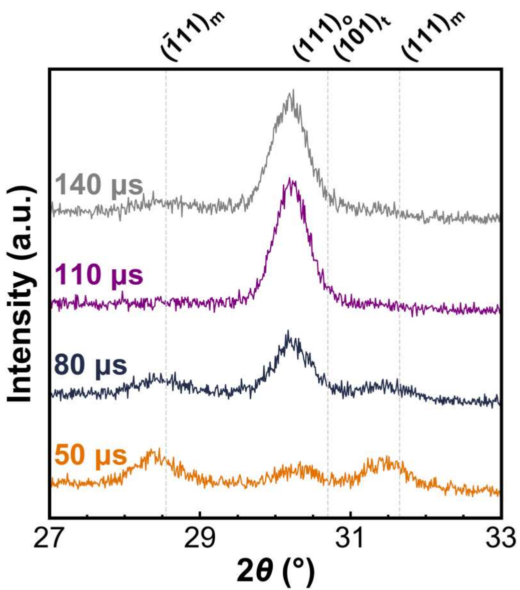

FIG. 6. In-plane XRD patterns for films deposited with 50, 80, 110, and 140 μs pulse widths.

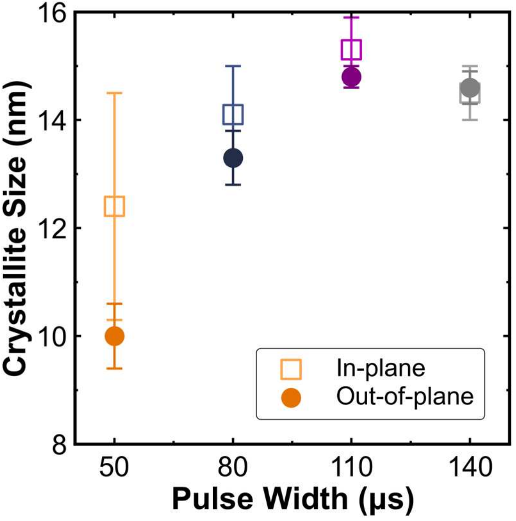

FIG. 7. Crystallite size calculated from in-plane and out-of-plane XRD measurements.

orthorhombic + tetragonal peak was used for these calculations, and this sample had the lowest fraction of the o + t phase and a lower signal-to-noise than the other films, which should result in smaller crystallite sizes. The other three pulse widths, 80, 110, and 140 μs, have more similar crystallite sizes from approximately 13–15 nm, with virtually no difference between the in-plane and out-of-plane dimensions.

The microstructure of the films was examined using plan-view SEM with images shown in Fig. S1 in the supplementary material.[31] Due to the small grain sizes and rapid carbon contamination of the samples under the electron beam, the resolution of the images is limited. Thus, AC mode AFM images were collected and are shown in Fig. 8. To quantify the lateral grain sizes, the lineal-intercept procedure was used,[27] and the mean intercept length is reported in Fig. 9, with error bars representing 95% confidence intervals. The intercept length is used as a proxy for the grain size in this work. The 50 μs sample has the largest grain sizes of 21.3 ± 0.8 nm. The 80, 110, and 140 μs samples have grain sizes of 17.9 ± 0.9, 17.3 ± 1.0, and 17.4 ± 1.4 nm, respectively. Although a small difference in the microstructure for the 50 μs sample was observed, overall, no clear trend could be established between the pulse width, grain size, phase, and electrical properties. More specifically, equivalent grain sizes were observed for the 80, 110, and 140 μs samples even though these samples had differences in the phase composition and electrical properties.

E. Discussion

In this work, it has been shown that varying the HiPIMS pulse width affects the phases that are formed during annealing. This effect does not appear to be tied to the microstructure since the grain size was shown to be relatively invariant. Therefore, a different aspect of the HiPIMS pulse width must be responsible. As previously mentioned, the positive ion-to-neutral ratio was inversely correlated to the pulse width. During these depositions, a positive pulse was applied after the negative pulse. This positive

27 July 2024 19:55:05

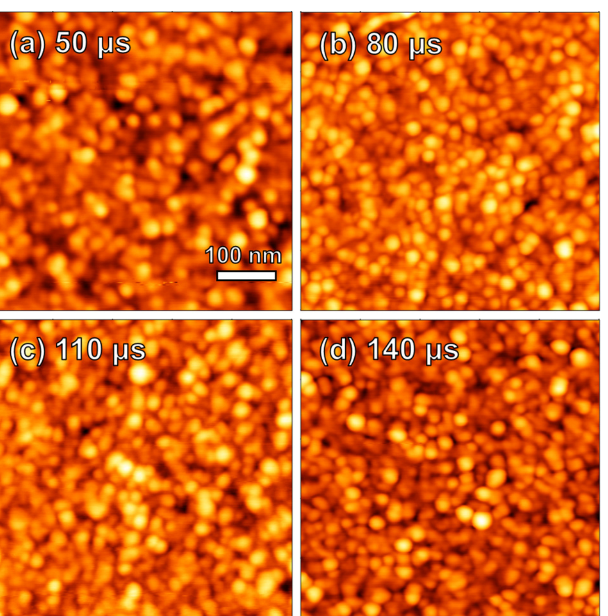

FIG. 8. AFM topography images of films deposited with (a) 50, (b) 80, (c) 110, and (d) 140 μs pulse widths.

Published under an exclusive license by the AVS

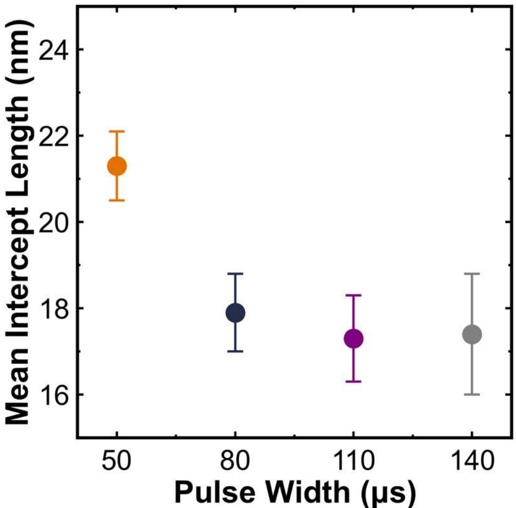

FIG. 9. Average lateral feature intercept length calculated using the lineal-intercept method on the AFM images with error bars representing 95% confidence intervals.

pulse will have the largest effect on plasmas with higher fractions of positive ions, resulting in greater ion bombardment of positive ions for lower pulse widths. It is hypothesized that these differences in ion bombardment affect the short-range order of the amorphous films through parameters like coordination and bonding environment, thereby affecting the nucleation behavior. Then, upon annealing, different phases are formed. Similar effects were observed in vanadium oxide films deposited with different PLD conditions—using grazing-incidence total x-ray scattering and pair distribution functions, the authors observed different local, short-range structures in the amorphous films of vanadium oxide deposited with different laser repetition rates. It was found that the starting amorphous structure influenced the phases that crystallized.[28] Additionally, different TiO_2 polymorphs were observed for films crystallized from deposits prepared under different PLD repetition rates and oxygen background pressures. The authors hypothesized that the residual strain in the amorphous deposit affected the local energy and nucleation kinetics.[29]

A similar phenomenon has also been observed in hafnium zirconium oxide films deposited by reactive RF magnetron sputtering with different working pressures in order to vary the energy of the incident species.[30] In this work, Bouaziz *et al*. demonstrated that a film deposited with high working pressure (low incident energy) contained more ferroelectric orthorhombic phase than a corresponding sample deposited with a low working pressure (high incident energy), which only contained the monoclinic phase. The authors suggested that this is because the high working pressure results in a structure closer to the amorphous phase present in ALD-processed films. Likewise, in the work presented here, the film deposited with the highest incident energy ($50\,\mu$s pulse width) had the highest fraction of the monoclinic phase. For metastable polymorphs like the polar orthorhombic phase in HfO_2, it is difficult to understand not only how the phase forms but also what approach(es) to use to stabilize it. These results suggest that controlling the short-range order in the amorphous structure via ion bombardment may enable the control of the phases that form and indicate a potential pathway for future study to prepare phase-pure ferroelectric hafnia.

IV. CONCLUSIONS

The effect of the HiPIMS pulse width on the nucleation, phase formation, microstructure, and ferroelectric properties of HfO_2 films deposited by HiPIMS has been demonstrated. *In situ* HTXRD measurements showed that the pulse width affects the nucleation temperatures of the phases in addition to phase stability. The heating rate did not have a significant impact on the crystallization of these films, although the heating rate has been shown to influence crystallization in ALD films. Differences in phase constitution were shown as the HiPIMS pulse width was varied, with the lowest pulse width, $50\,\mu$s, resulting in the largest fraction of the monoclinic phase present in these films. Although this sample had the largest average grain size of 21.3 ± 0.8 nm, the grain size was not shown to correlate with electrical properties. This is evident because the films deposited with 80, 110, and $140\,\mu$s pulse widths had similar grain sizes, but the $110\,\mu$s pulse width sample had a higher fraction of the o + t phases and a larger remanent polarization. These results demonstrate that while the HiPIMS pulse width does not significantly alter the microstructure that forms after high-temperature annealing, it has the ability to significantly affect the phases that form and the stability of these phases. It is hypothesized that the differences in ion bombardment with varying pulse widths drive changes in the short-range order of the amorphous film, which affects phase nucleation. Control of phase formation via a local structure in the amorphous state can, therefore, be used to fabricate HfO_2-based films with larger ferroelectric orthorhombic phase fractions and improved performance.

27 July 2024 19:55:05

ACKNOWLEDGMENTS

Thin film synthesis, GIXRD measurements, electrical characterization, and microstructure characterization were supported by the Semiconductor Research Corporation (SRC) within the Nanomanufacturing, Materials, and Processes (NMP) Program under Task No. 2875.001. Ion-to-neutral measurements were supported by the Center for 3D Ferroelectric Microelectronics (3DFeM), an Energy Frontier Research Center funded by the U.S. Department of Energy, Office of Science, Basic Energy Sciences under Award No. DE-SC0021118. S.T.J. acknowledges the support from the U.S. National Science Foundation's Graduate Research Fellowship Program under Grant No. DGE-1842490. K.G.O. and P.R. acknowledge the support by NSF DMR Metals and Metallic Nanostructures under Award No. 2004326. The HTXRD experiments were performed at the Analytical Instrumentation Facility (AIF) at North Carolina State University, which was supported by the State of North Carolina and the National Science Foundation (Award No. ECCS-2025064). The AIF is a member of the North Carolina Research Triangle Nanotechnology Network (RTNN), a site in the National Nanotechnology Coordinated Infrastructure (NNCI). This work was supported by the Laboratory Directed Research and

Published under an exclusive license by the AVS

Development Program at Sandia National Laboratories, a multimission laboratory managed and operated by National Technology and Engineering Solutions of Sandia LLC, a wholly owned subsidiary of Honeywell International Inc. for the U.S. Department of Energy's National Nuclear Security Administration under Contract No. DE-NA0003525.

AUTHOR DECLARATIONS

Conflict of Interest

The authors have no conflicts to disclose.

Author Contributions

Samantha T. Jaszewski: Conceptualization (equal); Formal analysis (equal); Funding acquisition (equal); Investigation (equal); Writing – original draft (equal). **Shelby S. Fields:** Investigation (equal); Writing – original draft (supporting). **Ching-Chang Chung:** Investigation (equal); Writing – original draft (supporting). **Jacob L. Jones:** Funding acquisition (supporting); Investigation (equal); Writing – original draft (supporting). **Keithen G. Orson:** Investigation (equal); Writing – original draft (supporting). **Petra Reinke:** Funding acquisition (supporting); Investigation (equal); Writing – original draft (supporting). **Jon F. Ihlefeld:** Conceptualization (equal); Formal analysis (equal); Funding acquisition (equal); Investigation (equal); Writing – original draft (equal).

DATA AVAILABILITY

The data that support the findings of this study are available from the corresponding author upon reasonable request.

REFERENCES

[1]T. S. Böscke, J. Müller, D. Bräuhaus, U. Schröder, and U. Böttger, Appl. Phys. Lett. **99**, 102903 (2011).
[2]K. J. Hubbard and D. G. Schlom, J. Mater. Res. **11**, 2757 (1996).
[3]H. A. Hsain, Y. Lee, M. Materano, T. Mittmann, A. Payne, T. Mikolajick, U. Schroeder, G. N. Parsons, and J. L. Jones, J. Vac. Sci. Technol. A **40**, 010803 (2022).
[4]V. Kouznetsov, K. Macák, J. M. Schneider, U. Helmersson, and I. Petrov, Surf. Coat. Technol. **122**, 290 (1999).
[5]A. Anders, J. Appl. Phys. **121**, 171101 (2017).
[6]A. Anders, Thin Solid Films **518**, 4087 (2010).
[7]J. Alami, K. Sarakinos, F. Uslu, and M. Wuttig, J. Phys. D: Appl. Phys. **42**, 015304 (2008).
[8]R. Materlik, C. Künneth, and A. Kersch, J. Appl. Phys. **117**, 134109 (2015).
[9]C. Künneth, R. Materlik, and A. Kersch, J. Appl. Phys. **121**, 205304 (2017).
[10]S. T. Jaszewski *et al.*, Acta Mater. **239**, 118220 (2022).
[11]J. Libra, KolXPD: Spectroscopy Data Measurement and Processing, https://www.kolibrik.net/en/solutions-products/kolxpd (2011).
[12]D. A. Shirley, Phys. Rev. B **5**, 4709 (1972).
[13]J. H. Scofield, J. Electron Spectrosc. Relat. Phenom. **8**, 129 (1976).
[14]P. Scherrer, Nachr. Ges. Wiss. Göttingen **2**, 96 (1918).
[15]D. R. Black, M. H. Mendenhall, C. M. Brown, A. Henins, J. Filliben, and J. P. Cline, Powder Diffr. **35**, 17 (2020).
[16]H. A. Hsain, Y. Lee, G. Parsons, and J. L. Jones, Appl. Phys. Lett. **116**, 192901 (2020).
[17]M. H. Park *et al.*, Adv. Electron. Mater. **4**, 1800091 (2018).
[18]D. Depla, X. Y. Li, S. Mahieu, and R. D. Gryse, J. Phys. D: Appl. Phys. **41**, 202003 (2008).
[19]A. Marcak, C. Corbella, T. de los Arcos, and A. von Keudell, Rev. Sci. Instrum. **86**, 106102 (2015).
[20]R. Ganesan, B. Akhavan, J. G. Partridge, D. G. McCulloch, D. R. McKenzie, and M. M. M. Bilek, J. Appl. Phys. **121**, 171909 (2017).
[21]T. Kubart and A. Aijaz, J. Appl. Phys. **121**, 171903 (2017).
[22]S. Suzer, S. Sayan, M. M. Banaszak Holl, E. Garfunkel, Z. Hussain, and N. M. Hamdan, J. Vac. Sci. Technol. A **21**, 106 (2003).
[23]A. Ferrec, J. Kéraudy, and P.-Y. Jouan, Appl. Surf. Sci. **390**, 497 (2016).
[24]R. P. B. Viloan, M. Zanáška, D. Lundin, and U. Helmersson, Plasma Sources Sci. Technol. **29**, 125013 (2020).
[25]G. Esteves, K. Ramos, C. M. Fancher, and J. L. Jones, LIPRAS: Line-profile analysis software (2017).
[26]V. K. Narasimhan, M. E. McBriarty, D. Passarello, V. Adinolfi, M. F. Toney, A. Mehta, and K. A. Littau, Phys. Status Solidi RRL **15**, 2000598 (2021).
[27]ASTM E112-13, *Standard Test Methods for Determining Average Grain Size* (ASTM International, West Conshohocken, PA, 2013).
[28]K. H. Stone, L. T. Schelhas, L. M. Garten, B. Shyam, A. Mehta, P. F. Ndione, D. S. Ginley, and M. F. Toney, APL Mater. **4**, 076103 (2016).
[29]J. S. Mangum, L. M. Garten, D. S. Ginley, and B. P. Gorman, J. Am. Ceram. Soc. **103**, 2899 (2020).
[30]J. Bouaziz, P. Rojo Romeo, N. Baboux, R. Negrea, L. Pintilie, and B. Vilquin, APL Mater. **7**, 081109 (2019).
[31]See the supplementary material online for plan-view SEM images.

27 July 2024 19:55:05

Published under an exclusive license by the AVS